Ultrasonics 99 (2019) 105964

Contents lists available at ScienceDirect

Ultrasonics

journal homepage: www.elsevier.com/locate/ultras

Angular and frequency behaviour of elastodynamic scattering from embedded scatterers

Jie Zhang[a,*], Maria V. Felice[a,b], Alexander Velichko[a], Paul D. Wilcox[a]

[a] Department of Mechanical Engineering, University Walk, University of Bristol, Bristol BS8 1TR, UK
[b] Present address: Proceq Asia Pte Ltd, 1 Fusionopolis Way, #20-02 Connexis South Tower, 138632 Singapore, Singapore

ARTICLE INFO

Keywords:
Scattering amplitude
Ultrasonic array
Forward model

ABSTRACT

The elastodynamic scattering behaviour of a finite-sized scatterer in a homogeneous isotropic medium can be encapsulated in a scattering matrix (S-matrix) for each wave mode combination. In a 2-dimension (2D) space, each S-matrix is a continuous complex-valued function of 3 variables: incident wave angle, scattered wave angle and frequency. In this paper, the S-matrices for various 2D scatterer shapes (circular voids, straight cracks, rough cracks and a cluster of circular voids) are investigated to find general properties of their angular and frequency behaviour. For all these shapes, it is shown that the continuous data in the angular dimensions of their S-matrices can be represented to a prescribed level of accuracy by a finite number of complex-valued Fourier coefficients that are physically related to the angular orders of the incident and scattered wavefields. It is shown mathematically that the number of angular orders required to represent the angular dimensions of an S-matrix at a given frequency is a function of overall scatterer size to wavelength ratio, regardless of its geometric complexity. This can be interpreted as a form of the Nyquist sampling theorem and indicates that there is an upper bound on the sampling interval required in the angular domain to completely define an S-matrix. The variation of scattering behaviour with frequency is then examined. The frequency dependence of the S-matrix can be interpreted as the Fourier transform of the time-domain impulse response of the scatterer for each incident and scattering angle combination. Depending on the nature of the scatterer, these are typically decaying reverberation trains with no definite upper bound on their durations. Therefore, in contrast to the angular domain, there is no lower bound on the sampling interval in the frequency domain needed to completely define an S-matrix, although some pragmatic solutions are suggested. These observations may help for the direct problem (computing ultrasonic signals from known scatterers efficiently) and the inverse problem (characterising scatterers from measured ultrasonic signals).

1. Introduction

The scattered ultrasonic wave-field from an object (a scatterer) contains a great deal of information about the geometry of the object. For quantitative non-destructive evaluation (NDE) of materials and structures, scattering is therefore of great interest for defect detection, characterisation and sizing [1]. Knowledge of elastodynamic scattering, either for bulk waves or guided waves, can be used for parametric studies to optimise defect inspection configurations with either single-element ultrasonic transducers [2] or ultrasonic arrays [3,4]. A thorough understanding of the direct scattering problem is also a necessary prerequisite for solving the inverse problem of obtaining defect geometry from the scattered wave-field, examples of which include defect characterisation using experimentally-measured scattered signals obtained from an ultrasonic array [5–8] and quantitative damage imaging using minimum sensor density [9,10].

The work described in the current paper was motivated in the first instance by the need to efficiently simulate scattered ultrasonic signals of arbitrary-shaped targets in the context of ultrasonic array data simulation. Fundamentally, this requires the simulation of data from every possible transmitter-receiver element combination, which is often termed the Full Matrix Capture (FMC) array data set [11]. At a particular scatterer, each transmitter-receiver element combination corresponds to a pair of incident and scattered wave directions. To simulate the FMC data associated with a particular scatterer, it is therefore necessary to compute the amplitude and phase of scattered signals over a range of different incident angles, scattered angles and frequencies. Traditionally, in direct numerical simulations such as Finite Element

* Corresponding author.
E-mail addresses: j.zhang@bristol.ac.uk (J. Zhang), mvfelice@gmail.com (M.V. Felice), a.velichko@bristol.ac.uk (A. Velichko), p.wilcox@bristol.ac.uk (P.D. Wilcox).

https://doi.org/10.1016/j.ultras.2019.105964
Received 4 June 2019; Received in revised form 13 July 2019; Accepted 16 July 2019
Available online 25 July 2019

(FE) methods, for different parameters in the modelled structure, for example, the geometry of the structure, the location of a transmitting array element, the orientation angle and location of a scatterer, a separate execution of the model is required. However, an alternative and generally more efficient way to simulate FMC data is to pre-compute the complete scattering behaviour of a scatterer for all possible incident and scattering angles over the frequency range of interest; this data is termed the scattering matrix (S-matrix) [5,12]. The efficiency of using a pre-computed S-matrix in array data simulations is based on the fact that the S-matrix is determined by the defect only and is independent on the array and inspection geometry parameters. The S-matrix can then be used in a ray-based hybrid model [4,12,13] to simulate the FMC data for that scatterer at any position and orientation relative to an array. The question is to determine the most efficient way to generate the S-matrix for an arbitrary scatterer. Typically frequency-domain FE techniques are employed [5,14–16]. Such FE models must be executed separately for a sufficient number of incident wave directions and frequencies. The computation burden of this type of modelling therefore depends on the execution time of each model and the angular and frequency sampling intervals required to capture all the information in the S-matrix. The latter factors are equivalent to the minimum number of angular positions and frequencies required to accurately characterise a scatterer to a known degree of accuracy in practice.

In this paper, the S-matrices of several shapes of 2D embedded scatterers are first calculated at very high fidelity in the frequency and angular domains using appropriate methods. Each embedded scatterer is assumed to exist in an unbounded domain and is defined by its shape and overall size. The angular and frequency dependencies of these S-matrices are then investigated, as are the angular and frequency sampling intervals required to accurately describe them. Only the S-matrix from longitudinal incident and scattered wave modes for 2D embedded scatterers are considered in this paper, but similar analysis could be applied to the S-matrices from other wave combinations and for 3D scatterers. It should be noted that the paper is not about which modelling method (FE or analytical solutions) is more efficient to calculate an S-matrix, but on how to use the chosen modelling method most efficiently by determining the minimum angular and frequency increments required to completely capture scattering behaviour.

2. Definition of S-matrix and its relationship to ultrasonic response

In this section, the S-matrix is formally defined and its relationship to the ultrasonic response of a scatterer is explained.

2.1. Definition of S-matrix

The interaction between ultrasonic waves and a 2D scatterer embedded in an infinite isotropic elastic medium is completely encoded in a set of S-matrices, one for each incident and scattered mode combination. For each combination, the S-matrix describes the far-field complex amplitude of scattered signals as a function of incident angle, scattered angle and frequency [5,12]. Fig. 1(a) shows a continuous plane wave of amplitude u_i incident on a 2D embedded scatterer at angle α, and the angle, β, of a scattered wave. The angles are with respect to the lateral axis of the coordinate system and are measured about the nominal centre of the scatterer. The scattered wave in the far-field decays in inverse proportion to the square root of the distance from the scatterer. If the far-field complex amplitude of the scattered wave measured at a distance r from the nominal centre of the scatterer is u_s, then the far-field S-matrix is defined as:

$$S(\alpha, \beta, f) = \frac{u_s}{u_i}\sqrt{\frac{r}{\lambda}}e^{-ikr} \tag{1}$$

where f is the frequency of excitation, λ is the wavelength and $k = 2\pi/\lambda$ is the wave number. Physically, the S-matrix describes the complex amplitude of the scattered cylindrical wave if was back-propagated to a distance of λ from the nominal centre of the scatterer. It is noted that the S-matrix is actually a continuous function of 3 parameters rather than a matrix; however, the term S-matrix has been used in the NDE field for a few years [5] and is used here for brevity. It should also be noted that the data in the S-matrix is equivalent to the many alternative scattering descriptions used by other authors, such as the far-field pattern [17], the transition or T-matrix [18], the scattering amplitude [19] and the directivity [20].

Exact analytical solutions for elastodynamic scattering problems are limited to those for certain geometrically-simple scatterer shapes such as smooth planar straight cracks [21–23] and circular holes [24]. Approximate solutions are also available under certain conditions. For example, if a scatterer is large and its shape slowly-varying compared to the elastodynamic wavelength, e.g. a smoothly curved crack, the Kirchhoff approximation [12,25,26] or the geometrical theory of diffraction (GTD) [13] may be applied. However, in reality, there are many scatterers of practical interest that have arbitrary shapes and for which there is no analytical model or appropriate approximate model available; the scattering in these cases can only be solved via direct numerical approaches such as finite elements (FE) [5,14,15,26], finite differences (FD) [16], boundary elements (BE) [27], etc.

2.2. Relationship between S-matrix and ultrasonic response of a scatterer

Consider an embedded 2D scatterer with its nominal centre at position $\mathbf{q}$, which is excited by waves generated by a transducer at point $\mathbf{u}$, as shown in Fig. 1(a). The time-domain response recorded by an identical receiving transducer at position $\mathbf{v}$, is defined as $e_s(\mathbf{u}, \mathbf{v}, t)$, where t is time. Assuming that the scatterer is in the far-field of both transducers, and that both transducers are in the far-field of the scatterer, the Fourier transform of $e_s$can be written as:

$$E_s(\mathbf{u}, \mathbf{v}, \mathbf{q}, f) = D(\mathbf{u}, \mathbf{q}, f)D(\mathbf{v}, \mathbf{q}, f)H(f)S(\alpha, \beta, f)e^{-2\pi i f(\tau_0(\mathbf{u},\mathbf{q})+\tau_0(\mathbf{v},\mathbf{q}))} \tag{2}$$

where $D(\mathbf{u}, \mathbf{q})$ describes the transducer directivity, beam spread and

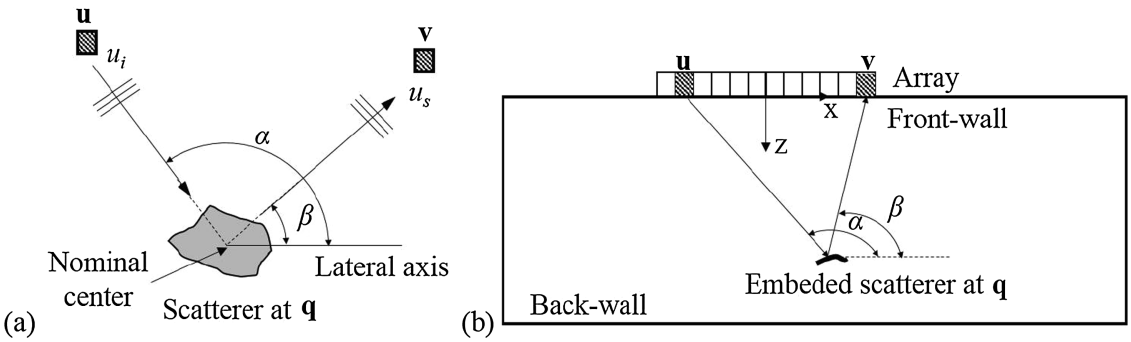

Fig. 1. Schematic diagrams illustrating notation used in (a) general model and (b) array data simulation of an embedded 2D scatterer with nominal center at **q**.

attenuation between a transducer at $\mathbf{u}$ and the point $\mathbf{q}$, $H(f)$ describes the frequency spectrum of the input ultrasonic pulse, $\tau_0(\mathbf{u}, \mathbf{q})$ is the ultrasonic transit time between $\mathbf{u}$ and point $\mathbf{q}$, and $S(\alpha, \beta, f)$ is the S-matrix of the scatterer. The angles α and β are determined by the positions $\mathbf{u}$, $\mathbf{v}$ and $\mathbf{q}$.

The previous expression can be re-written as

$$E_s(\mathbf{u}, \mathbf{v}, \mathbf{q}, f) = E_r(\mathbf{u}, \mathbf{v}, \mathbf{q}, f)S(\alpha, \beta, f) \tag{3}$$

where $E_r(\mathbf{u}, \mathbf{v}, \mathbf{q}, f)$ can be regarded as a reference response to a scatterer at point $\mathbf{q}$ that behaves as a perfect omni-directional target over all frequencies. In the time-domain, the above equation implies that the received signal can be written as a convolution:

$$e_s(\mathbf{u}, \mathbf{v}, \mathbf{q}, t) = e_r(\mathbf{u}, \mathbf{v}, \mathbf{q}, t) \otimes \ s(\alpha, \beta, t) \tag{4}$$

where $s(\alpha, \beta, t)$ is the inverse Fourier transform (with respect to frequency) of the S-matrix, $e_r(\mathbf{u}, \mathbf{v}, \mathbf{q}, t)$ is the inverse Fourier transform of $E_r(\mathbf{u}, \mathbf{v}, \mathbf{q}, f)$, and $\otimes$ is the convolution operator. This interpretation of the frequency-dimension of the S-matrix will be shown to have important consequences.

3. Analysis of s-matrix

In this section, the S-matrix behaviour as a function of scatterer size and shape is first demonstrated through the theoretical S-matrices from 5 representative scatterer types. The angular and frequency dependences of these S-matrices are then analysed. Finally, the application of S-matrices to simulating array data is introduced and the resultant ultrasonic image behaviour is analysed, as this was the original motivation for the work described in this paper.

3.1. Representative scatterer types

In order to investigate the scattering behaviour of general embedded scatterers, 5 representative types of scatterers of interest in NDE have been selected as shown in Fig. 2(a)–(e): a circular void, a cluster of 4 circular voids, a straight crack, a slightly rough crack and an extremely rough crack. The scatterer size a is defined by the smallest circumscribing circle that completely contains the scatterer; this is indicated by the dashed circles in Fig. 2(b)–(e) and in the case of the circular void in Fig. 2(a) this is simply the void diameter. The centres of these circles define the nominal centre of each type of scatterer. Four circular voids in type 2 scatterer have a same size as $a/4$ and are located randomly at $(0.37a,\ 0.06a)$, $(-0.33a,\ 0.18a)$, $(0.15a,\ 0.34a)$ and $(-0.06a,\ -0.37a)$ relative to the scatterer center. The scatterers are assumed to exist in homogeneous isotropic aluminium with a density of 2700 kg/m^3, a Young's modulus of 71 GPa, a Poisson's ratio of 0.34 and hence a longitudinal wave speed of $c = 6400$ m/s.

3.2. S-matrices of representative scatterer types

Exact analytical scattering solutions for a circular void [24] and a straight crack [22] exist and can be used to calculate benchmark S-matrices for these scatterers. However, there is no exact scattering solutions available for the other chosen scatterers. Instead, a local FE model [15,28] is used. For the high-fidelity benchmark S-matrix calculations described in this section, the incident and scattered angle ranges are from 0° to 360° with an angular interval of 1°. Each FE model execution yields the scattering coefficients for all scattering angles and a single incident angle. The model for each scatterer is therefore executed once for each incident angle to generate the full S-matrix.

Figs. 3 and 4 show the moduli of the S-matrices for the 5 scatterer types with sizes of $a/\lambda = 0.015$ and $a/\lambda = 10$ respectively. Particularly evident in Fig. 4 are the diagonal ridges that run along the straight lines $|\alpha - \beta| = 180°$ in all cases; these correspond to the shadowing effect of the scatterer on the opposite side to the incident direction. In the S-matrix for the planar crack shown in Fig. 4(c) there are also orthogonal diagonal ridges running along the straight lines $\alpha + \beta = 180°$ and $\alpha + \beta = 540°$, which correspond to specular scattering. Comparing the S-matrices in Figs. 3 and 4 for the same scatterer types, it can be seen that the smaller scatterers exhibit a reduced overall maximum scattering amplitude relative to the equivalent larger scatterers as well as more uniform scattered amplitudes over a wider range of angles. Comparison of the specular back-scattered ridges in the S-matrices for rough and smooth cracks of the same size, shown in Fig. 4(c) and (d) and 5(c) and (d), reveals a much less well-defined ridge for rough cracks. This can have the effect of either reducing or increasing the overall maximum scattering amplitude in the S-matrices [26,29,30].

3.3. Angular behaviour of S-matrices

Because the angular dependence of the S-matrix is periodic with interval 360°, it can be represented as a 2-dimensional Fourier series which contains the same information as the original S-matrix. The terms in the Fourier series representation correspond to scattering between different angular orders of the incident and scattered fields. In this section, the 2D Fourier series representations of the S-matrices from the 5 scatterer types are investigated to explore the maximum angular order of information present. A mathematical model is then proposed to explain the observed behaviour and to predict the maximum angular order required to accurately describe any S-matrix. The S-matrices from a large population of scatterers with various sizes are computed and used to validate the proposed model. Finally, a general angular sampling rule is proposed that can be applied to the S-matrix reconstruction for any scatterer.

3.3.1. Examples of Fourier series representation of S-matrix

For a specific frequency, the S-matrix as a function of incident and scattered angle can be represented as Fourier series [31]:

$$S(\alpha, \beta, f) = \sum_{m,n} A_{mn}(f) e^{i(m\alpha + n\beta)} \tag{5}$$

where m and n represent the incident and scattered angular orders respectively and the complex Fourier coefficient A_{mn} is given by

$$A_{mn}(f) = \frac{1}{4\pi^2} \int_0^{2\pi} \int_0^{2\pi} S(\alpha, \beta, f) e^{-i(m\alpha + n\beta)} d\alpha d\beta \tag{6}$$

The angular sampling interval required to accurately describe the S-matrix of a scatterer is determined by the number of terms needed in the summations in Eq. (5). Qualitatively, this is illustrated in Figs. 5 and 6, which show the moduli, $|A_{mn}|$, of the Fourier coefficients of the equivalent S-matrices in Figs. 3 and 4. If Figs. 5 and 6 are considered

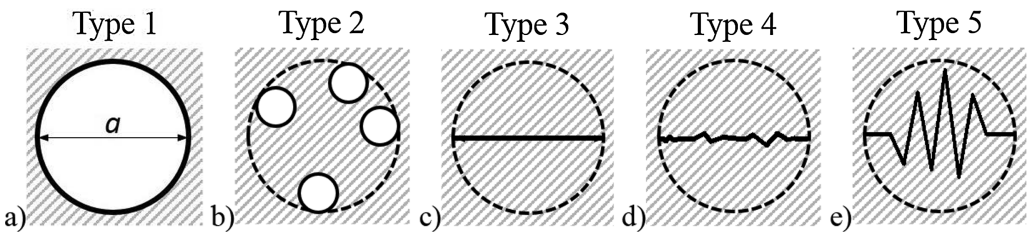

Fig. 2. The shape of a modelled: (a) circular void, (b) cluster of 4 circular voids, (c) straight crack, (d) slightly rough crack and (e) extremely rough crack.

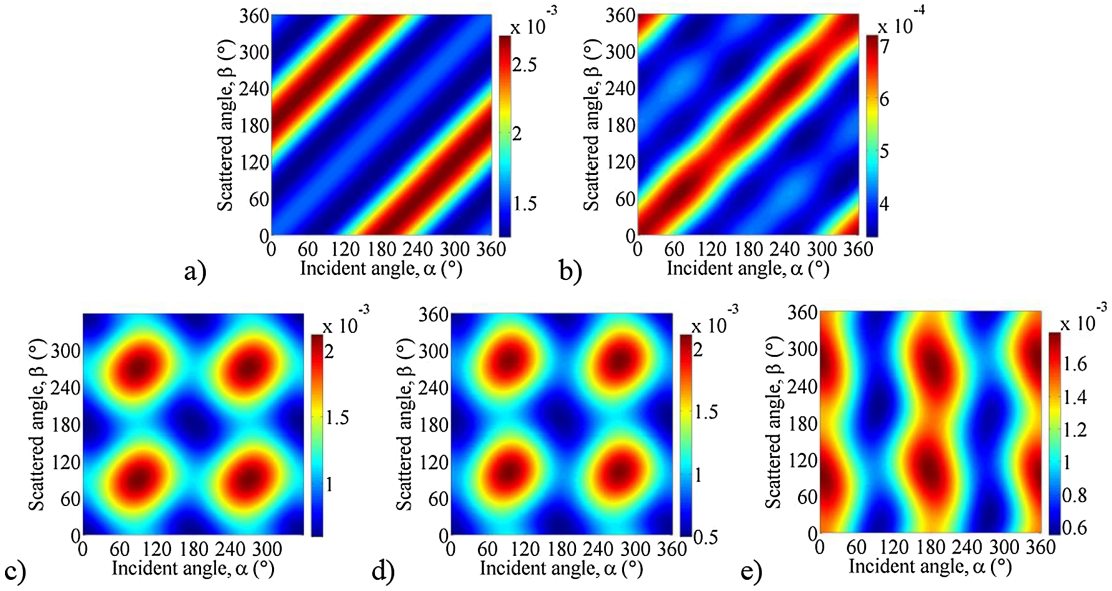

Fig. 3. Moduli of S-matrices of scatterers of size $a/\lambda = 0.015$ of (a–e) Type 1–5. Note that the colour-scale is linear.

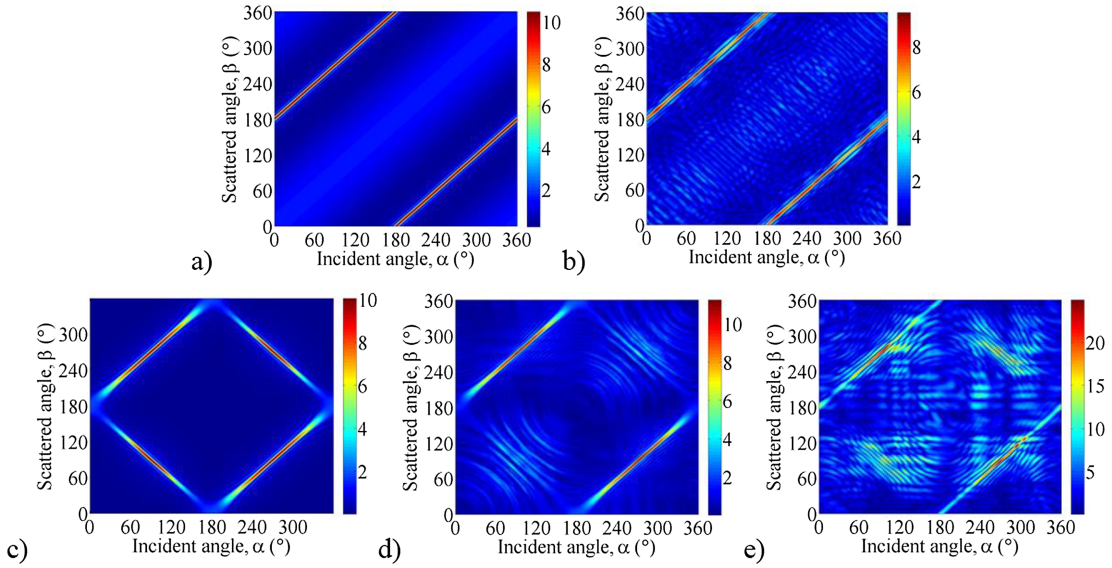

Fig. 4. Moduli of S-matrices of scatterers of size $a/\lambda = 10$ of (a–e) Type 1–5. Note that the colour-scale is linear.

separately, it can be seen that the maximum angular orders (i.e., the number of Fourier coefficients with amplitudes above a defined amplitude threshold) are similar for different types of scatterers of the same size. For example, for the scatterers with a size of $a/\lambda = 10$ shown in Fig. 6, a maximum angular order is $N = 37$ is sufficient to capture all Fourier coefficients with moduli greater than -40 dB (i.e. 1%) compared to the largest value. This suggests that for these scatterers, the S-matrices need to be computed at $2N + 1 = 75$ intervals between 0 and 360° in order to capture all the information in the S-matrix to order 1% accuracy. Comparing the Fourier coefficients in Figs. 5 and 6, it can be seen that a larger scatterer requires a higher maximum angular order and hence a smaller angular sampling interval.

3.3.2. Explanation for angular behaviour of S-matrix

Here the scalar wave equation is considered as it allows an algebraically simple description of the problem. However, the same results can be obtained by considering an elastic medium. The derivation in here is based on analysis of scalar wave, which could represent the acoustic case or the potential function describing an elastic wave. In the case of elastic waves, the scattered field contains both shear and longitudinal waves that need to be represented by two different potential functions. The analysis described here could be applied to either of these separately.

Referring to the schematic shown in Fig. 1(a), let the wave incident on a scatterer be a unit-amplitude plane wave with spatial dependence $\exp(i\mathbf{k}_\alpha \cdot \mathbf{r})$, where $\mathbf{k}_\alpha$ is the incident wave vector, $\mathbf{k}_\alpha = k\,[\cos\alpha \;\; \sin\alpha]^T$, and $\mathbf{r}$ is position relative to the nominal centre of the scatterer. The scatterer acts as a secondary source and generates a scattered wave field. This field from the secondary source can be represented by the field due to some distribution of forces, $F(\mathbf{k}_\alpha, \mathbf{r}')$, applied over a point at $\mathbf{r}'$ inside a scatterer-free medium. The scattered wave field at any position outside the scatterer area, $\mathbf{r} = r\,[\cos\beta \;\; \sin\beta]^T$ where r is the distance from the nominal centre of the scatterer and ~~is~~ β is the scattering angle relative to the lateral axis can then be written as the convolution integral

$$u_s(\mathbf{r}) = \int G_0(\mathbf{r} - \mathbf{r}')F(\mathbf{k}_\alpha, \mathbf{r}')d\mathbf{r}' \tag{7}$$

where $G_0(\mathbf{r}) = -\frac{i}{4}H_0^{(1)}(kr)$ is the 2D scalar Green's function of the

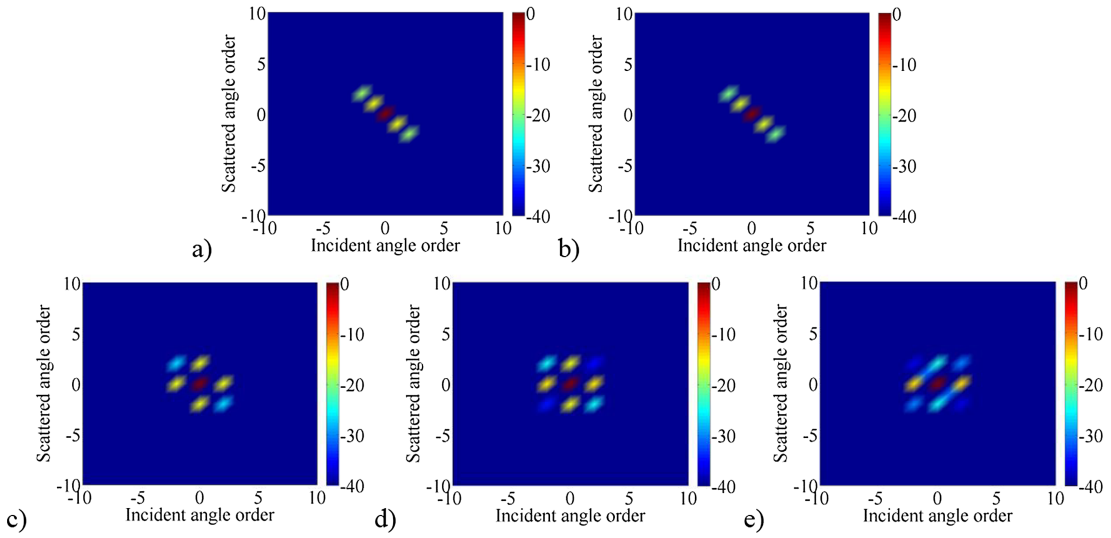

Fig. 5. Moduli of Fourier coefficients of the S-matrices shown in Fig. 3 for scatterers of size $a/\lambda = 0.015$: (a–e) Type 1–5. The colour scale is decibels relative to the largest coefficient in each case.

unbounded medium.

If $\mathbf{k}_\beta = k\mathbf{r}/r = k[\cos\beta \ \ \sin\beta]^T$ is defined as the scattered wave vector in the scattering direction β, then using the asymptotic form of the Hankel function $H_0^{(1)}$, the scattered wave in the far-field can be written as

$$u_s(\mathbf{r}) = -\frac{e^{\frac{i\pi}{4}}}{4\pi}\sqrt{\frac{\lambda}{r}}\,e^{i\mathbf{k}_\beta\cdot\mathbf{r}}\int F(\mathbf{k}_\alpha, \mathbf{r}')e^{-i\mathbf{k}_\beta\cdot\mathbf{r}'}d\mathbf{r}' = S(\alpha, \beta, f)\sqrt{\frac{\lambda}{r}}\,e^{i\mathbf{k}_\beta\cdot\mathbf{r}} \tag{8}$$

where the far-field S-matrix is

$$S(\alpha, \beta, f) = -\frac{e^{\frac{i\pi}{4}}}{4\pi}\int F(\mathbf{k}_\alpha, \mathbf{r}')e^{-i\mathbf{k}_\beta\cdot\mathbf{r}'}d\mathbf{r}' \tag{9}$$

The effective forces $F(\mathbf{k}_\alpha, \mathbf{r})$ can be written as a superposition of contributions from internal sources whose amplitudes are related to the incident field by

$$F(\mathbf{k}_\alpha, \mathbf{r}) = \int G(\mathbf{r}, \mathbf{r}')e^{i\mathbf{k}_\alpha\cdot\mathbf{r}'}d\mathbf{r}' \tag{10}$$

where $G(\mathbf{r}, \mathbf{r}')$ is the actual Green's function between two points in the unbounded medium containing the scatterer (i.e. not the Green's function for the scatterer-free unbounded medium, G_0). G contains all physical scattering processes that occur within the scatterer; for the purposes of this argument, it needs to exist but does not need to be known. Therefore, the S-matrix can be written in the general form,

$$S(\alpha, \beta, f) = -\frac{e^{i\pi/4}}{4\pi}\iint G(\mathbf{r}', \mathbf{r}'')e^{i(\mathbf{k}_\alpha\cdot\mathbf{r}'-\mathbf{k}_\beta\cdot\mathbf{r}'')}d\mathbf{r}'d\mathbf{r}'' \tag{11}$$

Using polar coordinates (r', θ'), (r'', θ'') in Eq. (11) and substituting into Eq. (6), the Fourier coefficients A_{mn} can be written as,

$$\begin{aligned} A_{mn} &= -\frac{e^{\frac{i\pi}{4}}}{16\pi^3}\int_0^{a/2} r'dr'\int_0^{a/2} r''dr''\int_0^{2\pi} d\theta' \\ &\quad \int_0^{2\pi} d\theta''[G(r', \theta', r'', \theta'')p_m(r', \theta')q_n(r'', \theta'')] \end{aligned} \tag{12}$$

where it is assumed that the scatterer is completely contained in a circle of diameter a and the functions p_m, q_n are given by,

$$p_m(r, \theta) = \int_0^{2\pi} e^{ikr\cos(\theta-\alpha)}e^{-im\alpha}d\alpha,\ q_n(r, \theta) = \int_0^{2\pi} e^{-ikr\cos(\theta-\beta)}e^{-in\beta}d\beta \tag{13}$$

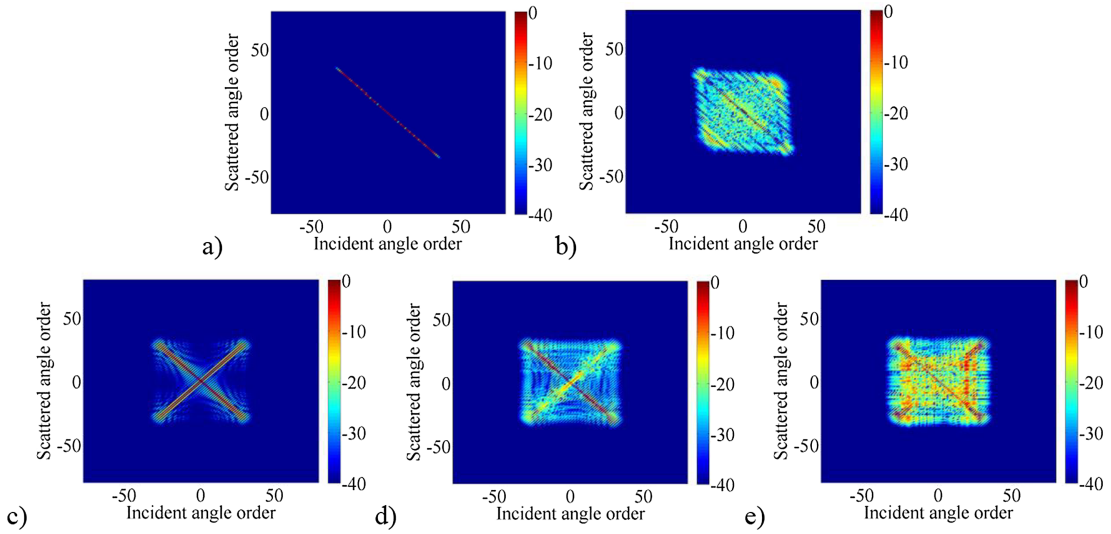

Fig. 6. Moduli of Fourier coefficients of the S-matrices shown in Fig. 4 for scatterers of size $a/\lambda = 10$: (a–e) Type 1–5. The colour scale is decibels relative to the largest coefficient in each case.

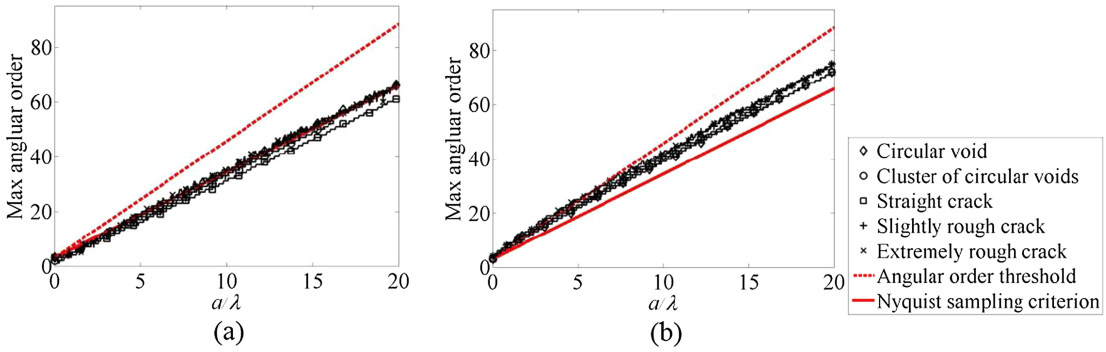

Fig. 7. Maximum angular order of Fourier coefficients of S-matrix as a function of scatterer size based on amplitude thresholds of (a) −20 dB and (b) −60 dB.

Using the relationship [34],

$$J_m(z) = \frac{e^{-im\pi/2}}{2\pi}\int_0^{2\pi} e^{iz\cos(\theta-\varphi)}e^{im\varphi}d\varphi \tag{14}$$

where J_m is Bessel function, Eq. (13) can be calculated as,

$$p_m(r,\theta) = 2\pi e^{-im(\theta-\pi/2)}J_m(kr),\ q_n(r,\theta) = 2\pi e^{in(\theta-\pi/2)}(J_m(kr))^* \tag{15}$$

where * is the conjugation operator. For large positive order the Bessel function can be approximately written as [34],

$$J_m(z) \approx \frac{1}{\sqrt{2\pi m}}\left(\frac{ez}{2m}\right)^m \tag{16}$$

Taking into account that $J_{-m}(z) = (-1)^m J_m(z)$ [34] the expression (12) can be estimated as,

$$|A_{mn}| \le \frac{G_M}{32}\frac{a^4}{(|m|+2)(|n|+2)\sqrt{|mn|}}\left(\frac{\pi ea}{2\lambda\ |m|}\right)^m\left(\frac{\pi ea}{2\lambda\ |n|}\right)^n \tag{17}$$

where $\lambda = 2\pi/k$ is the wavelength and $G_M$is the upper bound of the function $|G(\mathbf{r}', \mathbf{r}'')|$.

Both the terms $\left(\frac{\pi ea}{2\lambda\ |m|}\right)^m$ and $\left(\frac{\pi ea}{2\lambda\ |n|}\right)^n$ in (17) tend rapidly to zero when the quantity in parentheses is less than unity; in other words when $|m|$ or $|n|$ respectively exceed some critical value. Therefore an S-matrix can be efficiently represented by a limited number of terms in the expansion (1) for $|m,\ n| \le N$, where N is defined from the condition $\frac{\pi ea}{2\lambda} < 1$ as the maximum angular order required to accurately describe the wave fields, which depends on the size of the scatterer according to

$$N = \frac{\pi ea}{2\lambda} \tag{18}$$

The assumptions in the analysis means that the above expression is only valid in cases where N is large, i.e. for large scatterers when $a \gg \lambda$. For small scatterers the approximation breaks down and the above expression tends to zero. To include all scatterer size cases, it is proposed that a more generally applicable estimate of the upper bound of N is given by:

$$N = \frac{\pi ea}{2\lambda} + N_0 \tag{19}$$

where N_0 is the maximum angular order for sub-wavelength scatterers, $a \ll \lambda$. A numerical estimate for N_0 can be found from Fig. 5 as N_0 3 for all chosen smallest scatterers. The behaviour of the scattered waves from these smallest scatterers is a sum of elementary sources such as monopole ($m = n$=0), dipoles ($|m| = 1$, $|n| = 1$) and quadrupoles ($|m| = 2$, $|n| = 2$) [32]. This is similar to the three nonzero singular values of the scattering coefficients from a 2D elastic cylinder [33]. It is noted that, for an elastic wave in a homogeneous isotropic material, the appropriate Green functions, G, and elastic tensors should be used in Eq. (11) [12], but these do not change the exponential phase term, and hence do not affect the form of Eq. (17) so Eq. (19) is still valid. If the scattered waves are from wave mode conversion, then Eq. (19) can be applied to obtain the different upper bounds of N for the incident and scattered waves by using the appropriate wavelengths.

3.3.3. Angular sampling interval and S-matrix reconstruction in angular domain

Because the angular dependence of the S-matrix is periodic with interval 360°, Fourier interpolation can be used to reconstruct the S-matrix at any incident-scattered angle combination from the S-matrix values calculated at discretely-sampled points. The necessary sampling interval for S-matrix calculation is determined by the maximum angular order given by Eq. (19).

To validate the maximum angular order predicted by Eq. (19), a large population of benchmark S-matrices for the four scatterer shapes with sizes ranging from $a/\lambda = 0.015$ to 20 in 0.015 increments were simulated at high angular resolution (1° increments). The maximum angular order of each simulated S-matrix was then extracted using thresholds of −20 dB and −60 dB relative to the highest amplitude coefficient. As examples, the curves with symbols in Fig. 7(a) and (b) show the variation of maximum angular order of Fourier coefficient, N, with amplitude thresholds of −20 dB and −60 dB respectively, as a function of scatterer size, a/λ, for the chosen scatterers. As shown, the maximum angular order of Fourier coefficient starts at from a finite, non-zero value for the smallest scatterer size of $a/\lambda = 0.015$ (corresponding to the S-matrices shown in Fig. 5), and then monotonically increases with scatterer size. The trend is approximately linear with scatterer size and suggests that the number of angular orders required to characterise a scatterer of a given size can be readily estimated. Also shown in Fig. 7(a) and (b) is the dashed line obtained from Eq. (19), i.e., $N = \pi ea/2\lambda + N_0$, when $N_0 = 3$ corresponding to the largest angular order at the smallest straight crack size. For a similar problem, some researchers suggested using the Nyquist sampling criterion to decide the minimum number of angular observation required to decode the scattered field from a cylindrical scattering object with a diameter of a/λ [8,9,35]. This corresponds to the angular order of $N = \pi a/\lambda + N_0$ and the solid straight line in Fig. 7(a) and (b). Also from Fig. 7(a) and (b) it can be observed that the angular sampling interval depends on scatterer size.

From Fig. 7(a) and (b) it can be seen that the solid line obtained from the Nyquist sampling criterion matches the rate of increase in maximum angular order based on a −20 dB threshold, but underestimates the rate of increase for small scatterers if a −60 dB threshold is used. Conversely, the dashed line obtained from Eq. (19) matches the initial rate of increase in maximum angular order better if a −60 dB threshold is used, although it somewhat overestimates the maximum angular order for larger scatterers. It is suggested that Eq. (19) is used to obtain N, and hence a conservative estimate for the required angular sampling interval is:

$$\Delta\alpha = 360°/\left(\frac{\pi ea}{\lambda} + 2N_0 + 1\right) \tag{20}$$

It is noted that the traditional Nyquist criterion is derived by assuming that the spatial variability of the wavefield on the circle surrounding the defect and with the same radius as the defect (basically, on the defect surface) is equal to wavelength. However, this assumption is an approximation, because it ignores the nearfield effects. The criterion derived in this paper is based on rigorous mathematical analysis of the far-field S-matrix. It is shown that the angular spectrum of S-matrix has an infinite number of terms. However, these terms are very rapidly decreasing as their order increases, so, practically, only finite number of terms is needed for S-matrix reconstruction depending on the chosen accuracy threshold. For example, from Fig. 7 it is demonstrated that scattering information with amplitude above -20 dB of the maximum can be captured if the array sensors spacing is based on the Nyquist criterion. This is often adequate in practice. The angular sampling criterion defined in Eq. (20) suggests that more sensors can help to capture more scattering information, for example, that with amplitude above -60 dB of the maximum. It is also noted that the same conclusion can be deduced under the Born approximation [8], but our analysis is more general as it applies to any type of scatterer.

3.4. Frequency behaviour of S-matrices

In this section, the behaviour of S-matrices with respect to frequency is investigated. This behaviour is first demonstrated through the S-matrices for representative scatterers at a particular incident-scattered angle combination, by considering their inverse temporal Fourier transforms. The calculation error due to inadequate sampling frequency interval is analysed. Note that the benchmark S-matrices in Section 3.3.3, i.e., for the scatterers with sizes ranging from 0 to 20 a/λ with an increment of 0.015, are equivalent to the frequency-dependent S-matrices for scatterers of fixed size a over a frequency range from $f = 0$ to $20c/a$ with an increment of $\Delta f = 0.015c/a$.

3.4.1. Examples of frequency behaviour of representative S-matrices

Fig. 8(a)–(e) show examples of the real (solid lines) and imaginary (dashed lines) parts of a particular element in the S-matrices for the five types of scatterer as functions of frequency expressed in multiples of c/a. Fig. 8(c) is for $\alpha = \beta = 180^\circ$ while the other figures are for $\alpha = \beta = 90^\circ$. In all cases, the behaviour is a rapidly-changing function of frequency.

Fig. 9 shows the moduli of the inverse Fourier transform (IFT) of the corresponding functions in Fig. 8. These graphs are equivalent to the function $s(\alpha, \beta, t)$ in Eq. (4), in that they show the time-domain response of the scatterer at an angle β when a broadband pulse is incident at angle α. Note that corresponding to $\Delta f = 0.015c/a$ the actual time range of the IFT is from $t = -32.8a/c$ to $t = 32.8a/c$; however, Fig. 9 only shows the time range within $|t| \leq 5a/c$ to highlight earlier and high amplitude arrivals. In these graphs, time is expressed in multiples of a/c, which is physically the time taken for a wave to travel a distance equal to the size of the scatterer, a. The locations of the peaks relative to $t = 0$ correspond to the shifts in wave travel time due to the scatterer geometry. For example, the local peaks at time $t = -\frac{a}{c}$ that are visible in Fig. 9(a)–(c) correspond to the earliest possible arrival of waves scattered from a scatterer of size a compared to waves scattered from the nominal centre of the scatterer. Any non-zero signal at $t < -a/c$ is acausal and therefore non-physical. The time $t = -a/c$ corresponds to the earliest possible arrival of directly scattered waves, but the response signal can extend to $t > a/c$ due to reverberations within the scatterer. In Fig. 9(a)–(d), any such reverberations have decayed to a very low level by time $t = 5a/c$, while in Fig. 9(e) they have not. This is important, as the S-matrix sampling interval required in the frequency domain is determined by the maximum temporal extent of $s(\alpha, \beta, t)$ on either side of $t = 0$. For $t < 0$, this is bounded by the causal limit of $t = -a/c$, but for $t > 0$ the extent is determined by reverberations and therefore depends on the scatterer geometry. In fact, in the case of Fig. 9(e), the sampling interval in the frequency domain is inadequate; reverberant signals that would physically arrive at $t > 32.8a/c$ are wrapped in the time-domain and appear as non-physical signals that appear to arrive at $t < -a/c$.

It is noted that the reverberating waves may exist to some extent in any scatterer, for example, the creep waves from a circular void [24]. As reverberant waves decay exponentially to zero and therefore have infinitely long duration, the frequency sampling interval theoretically has to be infinitely small. With a finite frequency sampling interval, late arriving reverberations are wrapped in the time domain. Therefore, in practice, an amplitude threshold has to be defined in the time domain below in order to further analyse $s(\alpha, \beta, t)$. Here, $s(\alpha, \beta, t)$ was examined to determine the start time with a local peak amplitude, $t_1 < 0$, and end time with a local peak amplitude, $t_2 > 0$, of scattered signals for all incident and scattered angle combinations. For each angle combination, the times, t_1 and t_2, are calculated based on the earliest and latest instants at which the amplitude of $|s(\alpha, \beta, t)|$ is greater than -40 dB of the maximum value of $|s(\alpha, \beta, t)|$.

The results for the five scatterer types are shown in Fig. 10, which

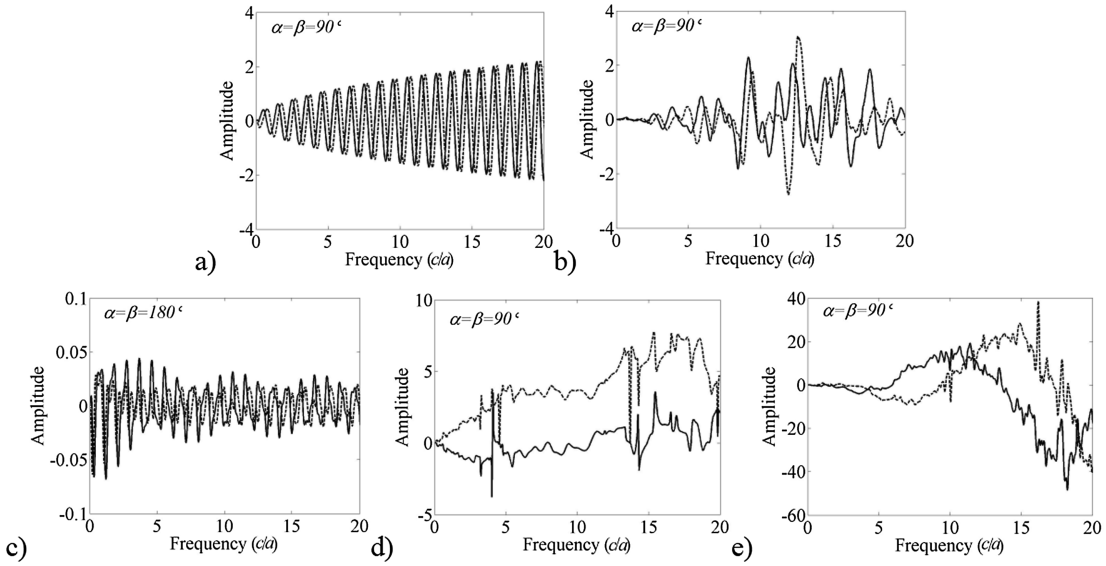

Fig. 8. Examples of the frequency behaviour of the real (solid lines) and imaginary (dashed lines) parts of particular terms in the S-matrices for scatterers of (a–e) Type 1–5.

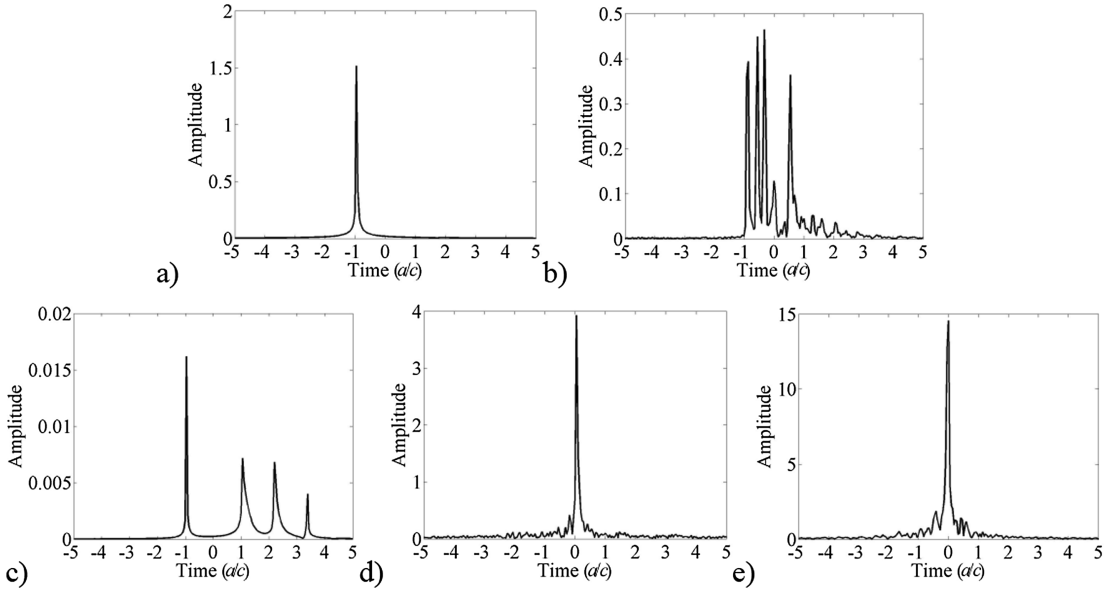

Fig. 9. Moduli of inverse Fourier transform (IFT) of example S-matrix terms shown in Fig. 8 for scatterers of (a–e) Type 1–5.

shows red if $t_1 < -a/c$, indicating the presence of non-physical, acausal signal. If $t_1 \geq -a/c$ the color represents whichever of t_1 and t_2 has the larger absolute value, (indicated by the other colours in which green and blue colours are for advanced arrival time and later arrival time respectively). It is evident from this figure that the behaviour of the five scatterer types is very different. In the case of the circular void shown in Fig. 10(a), there is negligible reverberation and $t_1 \geq -a/c$ and $t_2 < a/c$. Here, the largest time where the signal has significant amplitude is at $t_1 = -a/c$, and is where the back-scattered signal is advanced due to the reduced path length for reflections from the near edge of the void. In the case of a cluster of 4 circular voids, the advanced arrival signals and signals with short duration are mixed. In the case of the straight crack and the slightly rough crack, $|t_2| > |t_1|$ and the temporal extent of signals is governed by short duration time. However, for the extremely rough crack, red regions indicating the presence of acausal signals, which shows that the maximum duration that can be accommodated with the frequency sampling interval used in the simulation of even the benchmark S-matrices is inadequate.

3.4.2. *Frequency sampling interval in practice*

From the perspective of frequency-domain simulations of S-matrices, it would be attractive if the required sampling interval in the frequency domain could be estimated *a priori* in a similar manner to the angular sampling interval, which is governed by the maximum dimension of the scatterer. Unfortunately, the examples in the previous section suggest that there is no equivalent upper limit on the frequency sampling interval. Furthermore, even if the frequency sampling interval for a particular scatterer is determined, there is no exact interpolation scheme in the frequency-domain as the underlying functions are aperiodic; again this is in contrast to the Fourier interpolation that can be exploited in the angular domains due to periodicity. Instead, a cubic spline interpolation process for the frequency domain is proposed and its accuracy quantified.

Let the maximum duration of $s(\alpha, \beta, t)$ in the time-domain be T_0, indicated as the highest a/c for each scatterer type in Fig. 10. This implies that the maximum rate of change of $S(\alpha, \beta, f)$ in the frequency-domain is associated with oscillations that have a period of $\Delta f_0 = 1/T_0$. In order to adequately capture this information, the actual sample interval in the frequency domain, Δf, needs to be smaller that Δf_0. Fourier

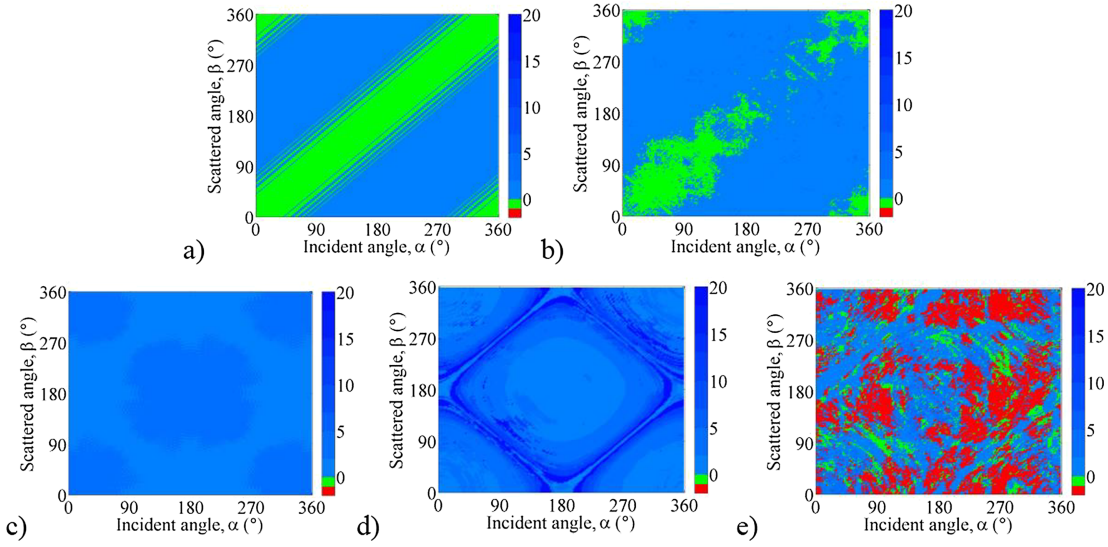

Fig. 10. Maximum or minimum time of IFT of S-matrices for scatterers of (a–e) Type 1–5. The color scales are in units of a/c.

Table 1
Simulated array parameters.

Array parameter	Value
Number of elements	64
Element width (mm)	0.53
Element pitch (mm)	0.63
Element length (mm)	15
Centre frequency (MHz)	5
Bandwidth (−6 dB) (MHz)	3–7

interpolation would require a sampling interval of $\Delta f \leq \Delta f_0/2$, but because $S(\alpha, \beta, f)$ is not periodic in f this is not an appropriate method. Instead, a local method is required, such as piecewise polynomial fitting. Here, cubic splines are used. It can be shown that if $\Delta f = \Delta f_0/7$, the maximum interpolation error is < 1% [36].

3.5. Ultrasonic signal simulation using S-matrices

Here, the examples of simulated A-scan time domain signals from the chosen scatterers are presented and analysed. An S-matrix frequency sampling rule for the purpose of simulating ultrasonic signals is suggested. In the simulations, the sound speed is $c = 6400$ m/s, the scatterers have a size of $a = 4$ mm and are aligned with the centre of the array in the depth direction in the modelled structure at (0, 20 mm) as shown in Fig. 1(b). The FMC data is simulated using Eqs. (2) and (3) and the benchmark S-matrices. Note that in these S-matrices, $\Delta\alpha = 1°$, $\Delta f = 0.015c/a$ for scatterers of type 1–5. It is noted that the portion of the S-matrices required is over the angular coverage range $135° \leq \alpha, \beta \leq 225°$ for the vertical straight crack and $45° \leq \alpha, \beta \leq 135°$ for the other scatterers. The specification of the simulated array is given in Table 1.

From Eq. (4), it can be seen that the times with a local peak amplitude in Fig. 9 are related to the phase shift of the scattered signal from a scatterer, e_s, relative to the reference signal, e_r, as shown in Fig. 11(a) which is a 5 cycle Gaussian-windowed toneburst and has a half width of $t_w = 0.8\ a/c$. This is demonstrated in Fig. 11(b)–(f) which show the examples of the simulated A-scan signals transmitted and received by the same centre array element from the simulated scatterers. In these figures, the dashed blue line in each figure indicates the arrival time of the corresponding reference signal, e_r. As shown in Fig. 11(b) for a circular void, a local peak amplitude at $t = -a/c$ in Fig. 9(a) causes a time shift of $-a/c$ of e_s relative to e_r. For the other scatterers, as shown in Fig. 11(c)–(f), the local peak amplitudes in Fig. 9(b)–(e) cause the multiple pulses around the arrival time of e_r. Note that the arrival time of a back-scattered reflection from a circular cavity, i.e., $-a/c$, should be the earliest physical time shift of any of the scattered signals from scatterers with a size of a. Comparing Fig. 9(e) with Fig. 11(f), it can be seen that the convolution process has suppressed some of the non-physical acausal signals although there are still some appearing at $t < -a/c$ in Fig. 11(f).

4. Reconstruction of s-matrix from limited data

In this section, the proposed guidelines for setting the angle and frequency sampling rates to accurately and efficiently reconstruct the scattered fields are examined and validated through the comparisons between the benchmark S-matrices and the reconstructed S-matrices, the benchmark TFM images and those generated using the reconstructed S-matrices.

4.1. Reconstruction of S-matrix in angular domain

An S-matrix with an angular sampling interval calculated according to Eq. (20) is computed first, and then the scattering amplitudes at any incident-scattered angles can be obtained using Fourier interpolation (Eqs. (5) and (6)). The accuracy of a reconstructed S-matrix can be examined by the root mean square (RMS) error,

$$\varepsilon_\alpha(\Delta\alpha_0, f) = \frac{\sqrt{\frac{1}{4\pi^2}\int_0^{2\pi}\int_0^{2\pi}[S_F(\Delta\alpha_0, f, \alpha, \beta) - S_B(f, \alpha, \beta)]^2 d\alpha d\beta}}{\frac{1}{4\pi^2}\int_0^{2\pi}\int_0^{2\pi}|S_B(f, \alpha, \beta)|\, d\alpha d\beta} \times 100\% \quad (21)$$

where S_B is a benchmark S-matrix obtained directly from the scattering model and S_F is the reconstructed S-matrix. The results obtained from all chosen scatterer types at all frequencies and $\Delta\alpha = 360°/\left(\frac{\pi e a}{\lambda} + 2N_0 + 1\right)$ show that $\varepsilon_\alpha \leq 1\%$ thus validating the proposed angular sampling interval rule.

4.2. Reconstruction of S-matrix in frequency domain

As discussed in Section 3.4, in the S-matrix reconstruction with respect to frequency, if the longest duration of scattered signals, T_0, can be estimated, then a frequency sampling interval of $\Delta f_0 = \frac{1}{7T_0}$ should

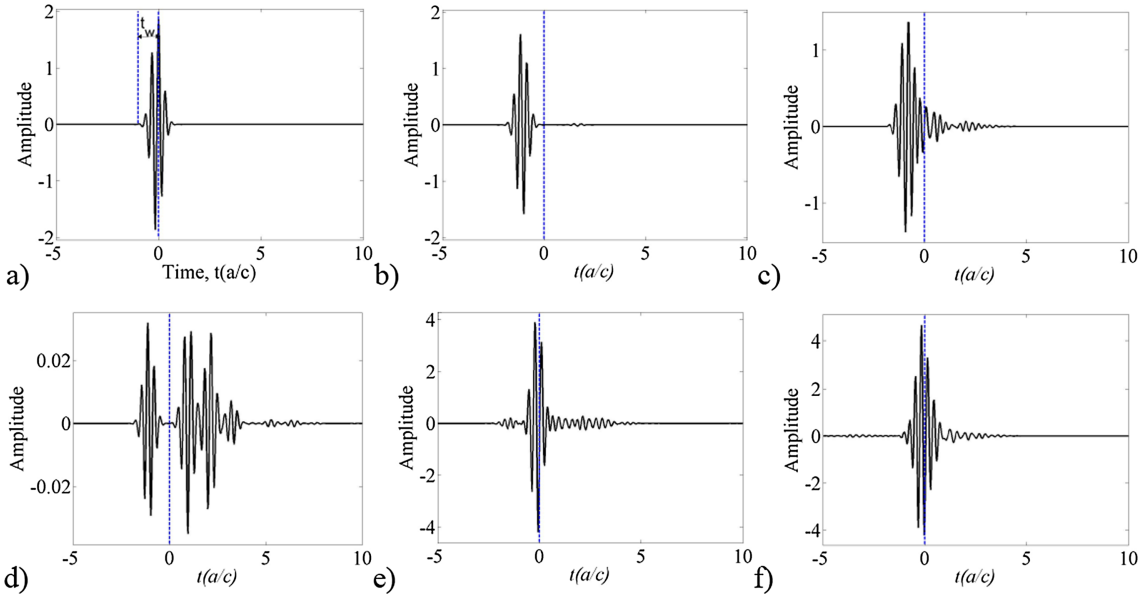

Fig. 11. (a) Reference signal, e_r, and examples of simulated A-scan signal from scatterers with shape type of (b–f) 1–5.

enable S-matrix values at any frequency to be obtained to with 1% accuracy using cubic spline interpolation. Here, this frequency sampling interval is first examined for the accuracy of the amplitude of the reconstructed S-matrices for the scatterers of types 1–3. The frequency sampling rule is then further discussed for application to simulating the response of an imaging algorithm. A method of determining the acceptable sampling frequency interval for S-matrix with unknown longest duration time is also suggested.

4.2.1. Considering the accuracy of the amplitudes in S-matrix

From Fig. 10(a)–(d), the longest duration time for type 1–4 scatterers can be extracted as, $T_0 = a/c$, $5a/c$, $4a/c$ and $25a/c$ respectively. The accuracy of the reconstructed S-matrix frequency obtained using the cubic spline interpolation method from the benchmark S-matrix with a frequency sampling interval of Δf_0 can be indicated by the RMS error,

$$\varepsilon_f(\Delta f_0, \alpha, \beta) = \frac{\sqrt{\frac{1}{f_m}\int_0^{f_m} [S_I(\Delta f_0, f, \alpha, \beta) - S_B(f, \alpha, \beta)]^2 df}}{\frac{1}{f_m}\int_0^{f_m} |S_B(f, \alpha, \beta)|\, df} \times 100\% \tag{22}$$

where f_m is the highest frequency used in the benchmark S-matrices. Note that the large red regions as shown in Fig. 10(f) indicate the frequency sampling interval used in the benchmark S-matrices for the type 5 scatterer (extremely rough cracks) is insufficient and the frequency interval in the benchmark S-matrices, $\Delta f = 0.015c/a$, is greater than $\Delta f_0 = 0.0057c/a$ for the type 4 scatterer, hence the reconstruction of such S-matrices is not considered in this section. In the reconstruction process, ε_f for scatterer types 1–3 over all incident and scattered angles was calculated. The results obtained from all scatterers at all incident-scattered angle combinations when $\Delta f_0 = \frac{1}{7T_0}$ show that $\varepsilon_f \leq 1\%$. This hence validates the S-matrix reconstruction using cubic spline interpolation in the frequency domain, provided that the appropriate frequency interval is used for the type of scatterer. Unfortunately, the appropriate frequency interval is not something that is known *a priori* for a scatterer.

4.2.2. Determination of the acceptable frequency sampling interval

In practical applications, such as non-destructive evaluation, the observed scattered wave fields comprise the impulse response of the scatterer convolved with a reference signal, e_s as modelled in Eq. (4) and as shown in Fig. 11. An inadequate frequency sampling interval causes non-physical signals that appear to arrive at $t < -a/c$ in Figs. 9(e), 10(e) and 11(f). These are associated with the rapidly-varying behaviour of the S-matrices with respect to frequency that can be seen in Fig. 8(e). To capture these variations requires a very fine sampling interval in the frequency domain. The acausal energy fraction in $e_s(\alpha, \beta, t)$ can be used to indicate the extent of acausal energy caused by the inadequate frequency sampling interval and it is defined as

$$\rho(\Delta f) = \frac{\iint_0^{2\pi} \int_{t_{min}}^{t_{min}+\frac{2a}{c}} |e_s(\alpha, \beta, t, \Delta f)|^2 dt d\alpha d\beta}{\iint_0^{2\pi} \int_{t_s}^{t_s+\frac{2a}{c}} |e_s(\alpha, \beta, t, \Delta f)|^2 dt d\alpha d\beta} \tag{23}$$

where t_{min} is the minimum time of the investigated S-matrices, $t_s = -\left(\frac{a}{c} + t_w\right)$. If the frequency sampling interval is adequate, ρ should be close to zero because energy at $t \leq t_s$ is acausal and non-physical.

Fig. 12(a) and (b) compare the acausal energy fraction, ρ, from the S-matrices for all scatterer types as a function of the frequency sampling interval under different e_r and t_w. e_r has 100% fractional −40 dB bandwidth but different central frequencies, i.e., $1.25c/a$ and $3.125c/a$, corresponding a pulse width of $t_w = 1.2\ a/c$ and $t_w = 0.48\ a/c$. At each specific Δf, the S-matrices used are a subset of the benchmark S-matrices ($\Delta f = 0.015c/a$) with a specific down-sampling rate (i.e. larger sampling interval). It is noted that t_{min} is limited by largest sampling interval in the analysis.

Fig. 12(a) and (b) show that the type 1–4 scatterers have low acausal energy fraction and become convergent at low Δf except some variations for type 2 scatterer when a higher frequency reference signal is considered in Fig. 12(b). It should be aware that non-monotonical trend from the acausal energy fraction, for example a few discrepancy points for type 5 scatterer at $\Delta f = 0.06c/a$, could indicate the local resonances of a scatterer. If it is happened in the bandwidth of e_r, the reverberation energy can be wrapped randomly in $t \leq t_s$ and break the monotonical trend of ρ as a function of Δf.

Combining the analysis in this section and the conclusion in Section 4.2.1, in practice, the convergence trend of the acausal energy fraction as a function of frequency interval can be used to determinate the acceptable frequency interval with regards to a defined e_r. In the process, the initial frequency interval can be set as $\Delta f = \frac{c}{7a}$ and then progressively reduced to the half of the previous Δf until the acausal energy fraction shows a convergence trend with low level ($\rho < 0.001$). It is difficult to make Δf indefinite small and acausal signals could hence be appear in the simulation, as shown in Fig. 11(f). However, in experiments, the non-physical acausal signals should not be appearance and the local resonance of a scatterer could cause a long duration rings. It is noted that, for the special cases to calculate S-matrices from types 1 and 3 scatterers, the frequency interval can be first set as $\Delta f = \frac{c}{7a}$ and $\frac{c}{28a}$ respectively, and then the cubic spline interpolation method can be used to calculate scattering coefficient at each required frequency.

5. Conclusion

It has been shown that the physical basis of the angular dependence of S-matrix is the integral of the large positive order Bessel function (Eq. (19)) as discussed in Section 3.3. The maximum angular order of Fourier coefficient needed to describe the angular dependence is dependent only on overall scatterer size and not on the scatterer type. This agrees with the findings of another study that showed that the minimum number of sensors required to monitor an area was determined by the diameter of the entire damage cluster [10]. The fact that at a single frequency, a behaviour of a scatterer can be characterised by a limited number of coefficients is a restatement of the finite number of degrees of freedom of a scatterer for both bulk waves [5] and guided waves [9,10]. At a single frequency, Fourier interpolation can be used to efficiently reconstruct the full S-matrix at all angles from S-matrix data obtained over a limited number of angles provided that these angles satisfy the necessary angular sampling rule.

From Eqs. (3) and (4), it is shown that the frequency-dependence of the S-matrix is what gives rise to the time-domain signature of a scatterer. As shown in Fig. 10, the maximum durations of scattered signals are highly dependent on the type of scatterer. This means that it is not possible to provide a general specification for the required frequency sampling interval in the same way that a required angle sampling interval can be specified; some types of scatterer have been shown to exhibit highly resonant behaviour leading to long duration signals in the time domain, which in turn requires very fine sampling intervals in the frequency domain to capture. Instead, the pragmatic solution is to use the acausal energy fraction metric to determine when an acceptable frequency interval has been reached.

The information in S-matrix with $|t| \leq a/c$ corresponds to scattering from spatial positions within the footprint of a scatterer (e.g. from the near side of a circular hole), therefore the frequency sampling interval must be at least sufficient to capture this. Information with $t > a/c$ is due to ringing within a scatterer and leads to a “tail” on time-domain signals. This is the true physical behaviour of the scattered signal in the time-domain. However, in simulation, an under-sampled S-matrix in the frequency-domain will lead to the information that should be in the tail of the time-domain signal being wrapped, polluting the true response and possibly leading to non-physical acausal signals.

The practical consequence of the findings may lead to more efficient

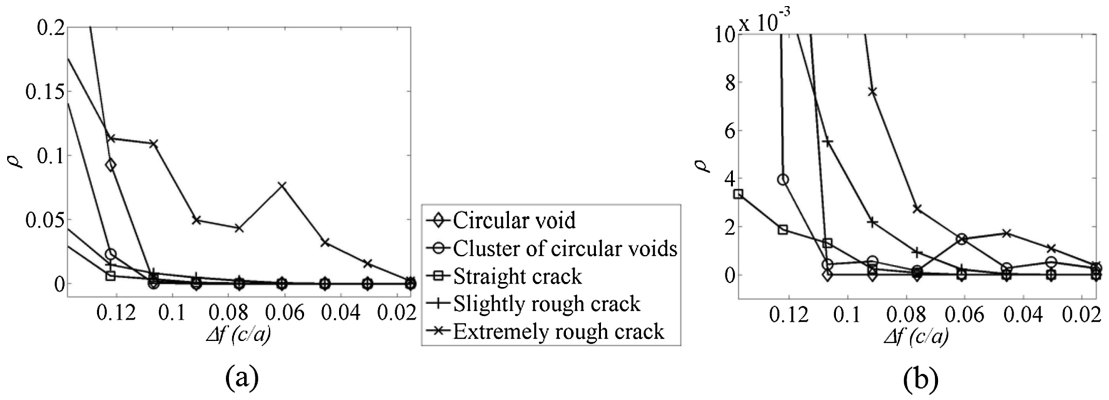

Fig. 12. The comparison of ρ as a function of the frequency sampling interval for types 1–5 scatterers using e_r with a central frequency of; (a and b) $1.25c/a$ and $3.125c/a$.

array data simulation (direct problem). For numerical simulations, the rules for determining the angular and frequency increments required to reconstruct an S-matrix enable minimisation of the number of numerical simulations needed to simulate an S-matrix and the amount of data needed for its storage. The angular and frequency increments relate to the maximum amount of information present in the scattered field. This knowledge in turn relates to how much information about the scatterer could be extracted from the scattered field by an inverse method.

It is also noted that, physical array design is currently based on choosing array parameters, such as frequency, aperture size, array element width and pitch, to achieve best detectability including good image resolution, less image artefacts from grating and side lobes and good signal to noise ratio. The work described in the paper can help to optimise array parameters for defect characterisation. For example, how to design an array to achieve best possible defect detection and characterisation through multi-view images [4,7].

Acknowledgements

This work was supported through the core research programme within the UK Research Centre in NDE (RCNDE) funded by EPRSC (grant number EP/L022125/1).

References

[1] J. Krautkramer, H. Krautkramer, Ultrasoinc Testing of Materials, Springer Verlag, New York, 2003.
[2] D.N. Alleyne, P. Cawley, Optimization of lamb wave inspection techniques, NDT & E Int. 25 (1992) 11–22.
[3] B.W. Drinkwater, P.D. Wilcox, Ultrasonic arrays for non-destructive evaluation: a review, NDT & E Int. 39 (2006) 525–541.
[4] J. Zhang, B.W. Drinkwater, P.D. Wilcox, A. Hunter, Defect detection using ultrasonic arrays: the multi-mode total focusing method, NDT & E Int. 43 (2010) 123–133.
[5] J. Zhang, B. Drinkwater, P. Wilcox, Defect characterization using an ultrasonic array to measure the scattering coefficient matrix, IEEE Trans. Ultrason. Ferroelectr. Freq. Control 55 (2008) 2254–2265.
[6] J. Zhang, B. Drinkwater, P. Wilcox, The use of ultrasonic arrays to characterize crack-like defects, J. Nondestruct. Eval. 29 (2010) 222–232.
[7] J. Zhang, T. Barber, A. Nixon, P. Wilcox, Investigation into distinguishing between small volumetric and crack-like defects using multi-view total focusing method images, in: AIP Conference Proceedings, AIP Publishing, 1806,040003, 2017.
[8] F. Simonetti, L. Huang, N. Duric, On the spatial sampling of wave fields with circular ring apertures, J. Appl. Phys. 101 (2007) 083103.
[9] C.H. Wang, L.R.F. Rose, Minimum sensor density for quantitative damage imaging, in: 9th International Workshop on Structural Health Monitoring, Stanford, USA, 2013, pp. 2248–2255.
[10] E. Chan, L.R.F. Rose, C.H. Wang, Sensor requirements for in situ imaging of multiple damage by lamb waves, Proceedings of the 11th Biennial Engineering Mathematics and Applications Conference, ANZIAM J. 55, Australian, 2014, pp. C282–C296.
[11] C. Holmes, B.W. Drinkwater, P.D. Wilcox, Post-processing of the full matrix of ultrasonic transmit-receive array data for non-destructive evaluation, NDT & E Int. 38 (2005) 701–711.
[12] L.W. Schmerr, Fundamentals of Ultrasonic Nondestructive Evaluation – A Modeling Approach, Prenum press, New York, 1998.
[13] J.D. Achenbash, A.K. Gautesen, H. McMaken, Ray methods for waves in elastic solids, Pitman Advanced Publishing Program, Prenum press, Boston, New York, 1992.
[14] P. Wilcox, A. Velichko, Efficient frequency-domain finite element modelling of two-dimensional elastodynamic scattering, J. Acoust. Soc. Am. 127 (2010) 155–165.
[15] A. Velichko, P. Wilcox, A generalized approach for efficient finite element modelling of elastodynamic scattering in two and three dimensions, J. Acoust. Soc. Am. 128 (2010) 1004–1014.
[16] M. Frehner, S.M. Schamholz, E.H. Saenger, H. Steeb, Comparison of finite difference and finite element methods for simulating two dimensional scattering of elastic waves, Phys. Earth Planet. Inter. 171 (2008) 112–121.
[17] D. Colton, J. Coyle, P. Monk, Recent developments in inverse acoustic scattering theory, SIAM Rev. 42 (2000) 369–414.
[18] A. Boström, H. Wirdelius, Ultrasonic probe modelling and non-destructive crack detection, J. Acoust. Soc. Am. 97 (1995) 2836–2848.
[19] F. Simonetti, Multiple scattering: the key to unravel to subwavelength world from the far-field pattern of a scattered wave, Phys. Rev. E 73 (2006) 036619.
[20] E.A. Skelton, R.V. Craster, A.V. Shanin, Embedding formulae for diffraction by non-parallel slits, Quart. J. Mech. Appl. Math. 61 (2007) 93–116.
[21] A. Boström, Review of hypersingular integral equation method for crack scattering and application to modelling of ultrasonic non-destructive evaluation, Appl. Mech. Rev. 56 (2003) 383–405.
[22] E. Glushkov, N. Gluskova, A. Ekhlakov, E. Shapar, An analytically based computer model for surface measurements in ultrasonic crack detection, Wave Motion 43 (2006) 458–473.
[23] E. Glushkov, N. Glushkova, M. Golub, A. Boström, Natural resonance frequencies, wave blocking, and energy localization in an elastic half-space and waveguide with a crack, J. Acoust. Soc. Am. 119 (2006) 3589–3598.
[24] A.L. Lopez-Sanchez, H. Kim, L.W. Schmerr Jr., A. Sedov, Measurement models and scattering models for predicting the ultrasonic pulse-echo response from side-drilled holes, J. Nondestruct. Eval. 24 (2005) 83–96.
[25] J.A. Ogilvy, Theory of Wave Scattering from Random Rough Surfaces, Adam Hilger, Bristol, 1991.
[26] J. Zhang, B. Drinkwater, P. Wilcox, Longitudinal wave scattering from rough crack-like defects, IEEE Trans. Ultrason. Ferroelectr. Freq. Control 58 (2011) 2163–2171.
[27] P.J. Schafbuch, F.J. Rizzo, R.B. Thompson, Boundary element method solutions for elastic wave scattering in 3D, Int. J. Numer. Meth. Eng. 36 (1993) 437–455.
[28] A. Velichko, P.D. Wilcox, An analytical comparison of ultrasonic array imaging algorithms, J. Acoust. Soc. Am. 127 (4) (2010) 2377–2384.
[29] A.J.C. Jarvis, F.B. Cegla, scattering of near normal incidence SH waves by sinusoidal and rough surface in 3-D: comparison to scalar wave approximation, IEEE Trans. Ultrason. Ferroelectr. Freq. Control 61 (2014) 1179–1190.
[30] F. Shi, W. Choi, M.J.S. Lowe, E.A. Skelton, R.V. Craster, The validity of Kirchhoff theory for scattering of elastic waves from rough surfaces, Proc. R. Soc. A 471 (2014) 20140977.
[31] G.P. Tolstov, Fourier Series, Prentice-Hall Inc, New Jersey, 1962.
[32] J.M. Charap, Covariant Electrodynamics – A Concise Guide, The Johns Hopkins University Press, Baltimore, 2011, p. 122 (Chapter 11).
[33] J. Minonzio, C. Prada, D. Chambers, D. Clorennec, M. Fink, Characterization of subwavelength elastic cylinders with the decomposition of the time-reversal operator: theory and experiment, J. Acoust. Soc. Am. 117 (2) (2005) 789–798.
[34] M. Abramowitz, I.A. Stegun, Handbook of Mathematical Functions, Dover Publications Inc, New York, 1970.
[35] F. Lin, A.I. Nachman, R.C. Waag, Quantitative imaging using a time-domain eigenfunction method, J. Acoust. Soc. Am. 108 (2000) 899–912.
[36] F.R. Moore, Table lookup noise for sinusoidal digital oscillators, Comput. Music J. 1 (1977) 26–29.